Self-Powered Portable Nanowire Array Gas Sensor for Dynamic NO_2 monitoring at room temperature

Shiyu Wei, Zhe Li, Krishnan Murugappan, Ziyuan Li, Fanlu Zhang, Aswani Gopakumar Saraswathyvilasam, Mykhaylo Lysevych, Hark Hoe Tan, Chennupati Jagadish, Antonio Tricoli*, and Lan Fu**

S. Wei, F. Zhang, Dr. Z. Y. Li, Prof. H. H. Tan, Prof. C. Jagadish, Prof. L. Fu
Australian Research Council Centre of Excellence for Transformative Meta-Optical Systems, Department of Electronic Materials Engineering, Research School of Physics, The Australian National University, Canberra, ACT 2601, Australia

Dr. Z. Li and A. G. Saraswathyvilasam
Department of Electronic Materials Engineering, Research School of Physics, The Australian National University, Canberra 2601, Australia

Dr. M. Lysevych
Australian National Fabrication Facility, The Australian National University, Canberra 2601, Australia

Dr. K. Murugappan
Nanotechnology Research Laboratory, Research School of Chemistry, College of Science, The Australian National University, Canberra 2601, Australia
Commonwealth Scientific and Industrial Research Organisation (CSIRO), Mineral Resources, Private Bag 10, Clayton South, Victoria, 3169, Australia

Prof. A. Tricoli
Nanotechnology Research Laboratory, Faculty of Engineering, The University of Sydney, Camperdown 2006, Australia
Nanotechnology Research Laboratory, Research School of Chemistry, College of Science, The Australian National University, Canberra 2601, Australia
E-mail: zhe.li@anu.edu.au; antonio.tricoli@anu.edu.au; lan.fu@anu.edu.au

Keywords: Self-powered, p-n homojunction, InP nanowire, gas sensor

Abstract

The fast development of Internet of Things (IoT) has driven an increasing demand of low-power consumption devices like self-powered gas sensors for real-time data collection and autonomous response in applications of environmental monitoring, industrial safety, smart cities and personal healthcare. Despite intensive research and rapid progress, most of reported self-powered devices, in particular NO_2 sensors for air pollution monitoring, suffer from limited sensitivity, selectivity and/or scalability issues. Here, a novel photovoltaic self-powered NO_2 sensor is demonstrated based on axial p-i-n homojunction InP nanowire (NW) arrays, targeting to break through these limitations. The optimized innovative InP NW array device is designed by numerical simulation for insight into sensing mechanism and performance enhancement. Without power source, this InP NW sensors achieve 84% sensing response to 1 ppm NO_2 and record limit of detection down to sub-ppb level with little dependence of the light intensity even under <5% of 1 sun illumination. Based on this great atmosphere light fidelity, the sensor is integrated onto a commercial microchip interface for dynamic self-powered monitoring of on-field motor vehicle exhaust. Our work indicates that compound semiconductor nanowires form promising sensing platforms, achieving self-powered, high performance, miniaturized sensor networks for future mega-scale IoT systems.

1. Introduction

The large-scale implementation of Internet of Things (IoT) technology over the recent decade has driven great demand for reliable and accurate gas sensor networks aiming at real-time data collection and autonomous response in applications such as air pollution monitoring, industrial chemical hazard detection, smart cities and personal healthcare.[1-2] Given the immense amount of sensors required to feed into this network, it is ideal to attain sensor characteristics such as micro/nano-size, superior sensitivity and detectivity, fast response, and orders of magnitude less power consumption than current commercial devices.[3-4] Conventional battery-powered sensors not only require continuously power supply during operation, but also are difficult to miniaturize for highly integrated systems.[5-6] Self-powered sensing systems are one of the most promising solutions to overcome power supply issue and achieve miniaturization.[7-9] Such systems can harvest energy from the environment such as sunlight, body motion, and heat, to realize zero-power consumption.[6, 10] Among these different types of self-powered gas sensors, photovoltaic (PV) effect based sensors are under active research, as PV effect and gas sensing function can be achieved simultaneously within the same junction or semiconductor active

layer.[11] This simplified structure enables low-cost and less complicated fabrication processes, which are desirable for integration into next generation IoT system.[12]

Over the past decade, self-powered PV gas sensors have been demonstrated by forming p-n or Schottky junctions based on a variety of bulk or low-dimensional materials, including 2D materials (graphene, WS_2, WSe_2),[13-14] metal oxide,[15] perovskite,[16] carbon nanotube,[17] and hyper-doped Si[18-19]. However, most of the reported self-powered gas sensors show issues such as limited sensitivity and selectivity at room temperature,[20] signal drifts and lack of stability over time,[21-22] as well as challenges in integration with complementary metal-oxide-semiconductor (CMOS) based technology.[16]

III-V compound semiconductors are the key materials for record-efficiency single- and multi-junction solar cells,[23] due to their direct tuneable bandgap, superior optical and electronic properties. Specifically, III-V nanowires (NWs), as one of the most studied nanostructures, have been demonstrated as a promising candidate for PV solar cell applications.[24-25] Moreover, the capacity to grow III-V NWs on silicon substrates provides enormous potential for integration with the existing silicon-based CMOS infrastructures.[26-27] Even though the PV effect is readily available in III-V NWs which also have been applied in several gases and biomolecules sensing studies,[28-29] they have rarely been investigated for the self-power gas sensors. Recently, our group has reported for the first time that ,a room-temperature indium phosphide (InP) NW array sensor, which, by careful optimization of the nanowire array design and top-down fabrication, has achieved parts-per-billion (ppb) level sensitivity and high selectivity towards Nitrogen dioxide (NO_2) with fast response (response time < 50 s).[30]

In this work, we report a novel InP NW array-based gas sensor architecture that combines PV junction and active sensing region to achieve highly sensitive, selective, and reproducible self-powered NO_2 sensing at room-temperature. Prior to NW growth, the NW and device structure were designed via numerical simulation that models PV NW sensing mechanism and optimizes performance. Then p-i-n junction InP NW arrays were grown according to the simulation optimized structure by selective-area metal-organic vapor-phase epitaxy (SA-MOVPE).[31] The NW crystal structure and optical property were characterised by transmission electron microscopy (TEM), photoluminescence (PL) and time-resolved photoluminescence (TRPL). The NW array sensor devices were designed and fabricated to enable robust contacts for signal extraction, while maintaining a large exposed NW active area for gas sensing. Without an

external power source, the device operates as photovoltaic gas sensor and responds to NO_2 with a highly sensitivity even under a much weaker light intensity than standard solar simulator, selectivity, and a sub-ppb level limit of detection (LOD). Finally, we demonstrate that our NW sensor can be readily integrated onto a microchip board for on-field dynamic NO_2 concentration measurement from vehicle exhaust pollutant. Our results and findings pave the way towards a miniaturized, power source-free nanoscale sensor platform for future IoT system applications.

2. Results and Discussion

2.1 Device Design and Self-Powered Sensing Mechanism

When applied to gas sensing, the one-dimensional nanoscale NW geometry provides abundant and engineerable surface area for adsorbing and interacting with gas molecules. For an InP NW array, it is found that once the NO_2 molecules are adsorbed onto the NW surface, the resultant acceptor-like surface states capture electrons from the NW surface,[32] turning it into a high resistance state and leading to a measurable signal of the adsorbed NO_2. Based on this fundamental mechanism and PV effect attainable by formation of a p-n junction, we have conceptualized an InP NW array PV sensor to achieve gas sensing and self-powered carrier collection simultaneously. Under light illumination, a photocurrent is generated in the p-n junction embedded NWs i.e., a short-circuit current (I_{SC}) without externally supplied power. NO_2 exposure effectively modulates the photocurrent flowing through the p-n junction due to the charge (electrons) transfer from the NWs to the adsorbed NO_2 molecules, causing significant change of the photocurrent. Therefore, the p-n junction-based sensing response (R) can be defined as:

$$\mathrm{R} = \frac{\left(I_0 - I_{\mathrm{gas}}\right)}{I_0} \times 100\% \qquad (1)$$

where I_0 and I_{gas} denote the initial I_{SC} in air and the final I_{SC} in response to gas adsorption, respectively. I_{gas} can be either greater or smaller than I_0 as will be discussed later, leading to either a positive or negative value for the measured R.

To better understand the PV NW sensing mechanism, we investigated and compared two common axial p-n junction structures, based on material growth which has been extensively studied and optimized in our previous work[25, 31, 33]: NW array with i-(intrinsic) and n-doped segments grown on a p-doped InP substrate, referred as p-i-n hereafter (**Figure 1**a), and NW array with i-(intrinsic) and p-doped segments grown on a n-doped InP substrate, referred as n-

i-p hereafter (Figure 1b). To allow effective gas sensing and NW top contact for signal extraction, a light illumination window is created at the top of the NW for gas exposure (Figure 1a). Considering mechanical stability of the NW array, the size of exposure window cannot be too large and is set to 700 nm in the simulation, which is a realistic size that can be achieved reliably by device fabrication. By varying the top i-n or i-p junction depth of these two types of NW structures shown in Figure 1a, b, we simulated I_{SC} before and after gas exposure to calculate sensing response by Equation 1 using COMSOL Multiphysics (see Figure S1, section 1 in Supporting Information (SI) for details of model setup).

It is found that the relative position of i-n or i-p junction with respect to the exposure window plays a critical role in sensing performance, as plotted in Figure 1c, d, respectively. For p-i-n structure, large positive responses are obtained as shown in Figure 1c, whereas for n-i-p structure, the response changes from positive to negative within a small range of values with the junction depth increasing as shown in Figure 1d. The polarity of the sensing response for different structures can be explained with the aid of a band diagram of the NW top junction (Figure 1e, f), where the case of n-/p-doped top segment length is exemplarily set as 450 nm. For the case of a p-i-n structure under illumination, NO_2 gas molecules adsorbing on the top n-doped segment and i-region of the NW (lightly n-doped due to background impurity doping during SA-MOVPE growth based on experimental data[24]) will form surface states that act as electron acceptors, giving rise to an upward surface band bending as shown in Figure 1e.[34-35] As a result, the majority carrier (i.e. electron) concentration in both top n-doped segment and i-region is reduced, leading to decreased photocurrent and hence a positive sensing response as calculated by Equation 1. Since the top n-segment is highly doped to 3×10^{18} cm^{-3}, the corresponding band bending (and carrier depletion) is much less evident than that in the i-segment subject to same amount of gas adsorption. Therefore, the sensing response of p-i-n structure decreases sharply as the top n-segment length increases until longer than exposure window where no i-segment is exposed for sensing, since most carrier depletion occurs within the i-layer.

When a n-i-p NW sensor is exposed to NO_2, the resultant upward band bending (Figure. 1f) in the top p-doped segment increases majority carrier (i.e. hole) concentration and thus photocurrent shows an enhancement; whereas in i-region the band bending depletes majority carriers (i.e. electron), leading to decreased photocurrent in contrast to the p-segment. For a shallow i-p junction as Figure 1f, due to the large band bending in the i-segment, electron

depletion plays a dominant role than the hole enhancement in the top p-doped segment. The net effect leads to a decreased photocurrent and positive sensing response. As the junction depth increases, hole concentration enhancement becomes increasingly larger, which eventually leads to increased photocurrent and thus a negative sensing response. By comparing the response curves for the two structures, it is clear that the p-i-n based device is a better candidate for high-performance oxidative gas sensing. The length of top junction plays a critical role, which should be kept as short as possible just for the electrical contact, so that i-region can be sufficiently exposed for better sensing performance. For n-i-p structure, on the other hand, varying junction depth plays limited role due to its bipolar sensing response in top p-segment and i-region. As a result, the (absolute value) response is less than 5% with all junction depths considered.

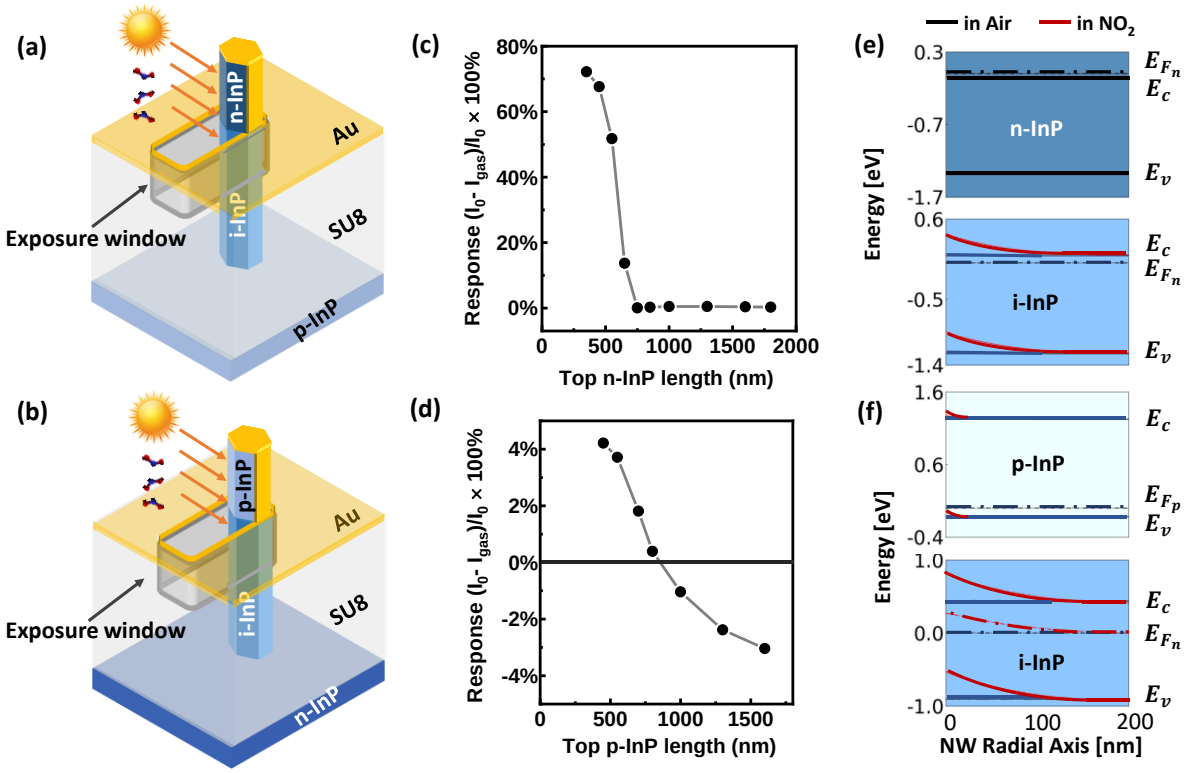

Figure 1. (a, b) Three-dimensional schematic of a unit cell of p-i-n and n-i-p NW based sensor, respectively. (c, d) Simulated gas sensing response vs NW top segment length. (e, f) Band diagram of the respective structures before (i.e. in air) and after gas exposure (i.e. in NO_2). Due to the background impurity doping, the unintentionally doped i-segment grown by SA-MOVPE is normally n-type (n^-).[24]

2.2 Experimental Results and Discussion

To confirm the simulation results, two types of axial homo-junction InP NW structures, p-i-n and n-i-p, illustrated in **Figure 2**a, e, were grown by SA-MOVPE (see details in Figure S2, SI

section 2) under the same conditions reported previously[33].The scanning electron microscope (SEM) images shown in Figure 2b, c, f, and g, highlight the well-ordered InP NW arrays with taper-free hexagonal-cylinder shape. The two structures display a similar configuration due to the same growth time and substrate pattern design, with a diameter of around 110 nm, a length of 3-4 µm, and the inter-spacing of 600 nm. The crystal structure is determined by transmission electron microscopy (TEM) analysis, confirming a pure wurtzite crystalline structure (Figure S3 in SI).

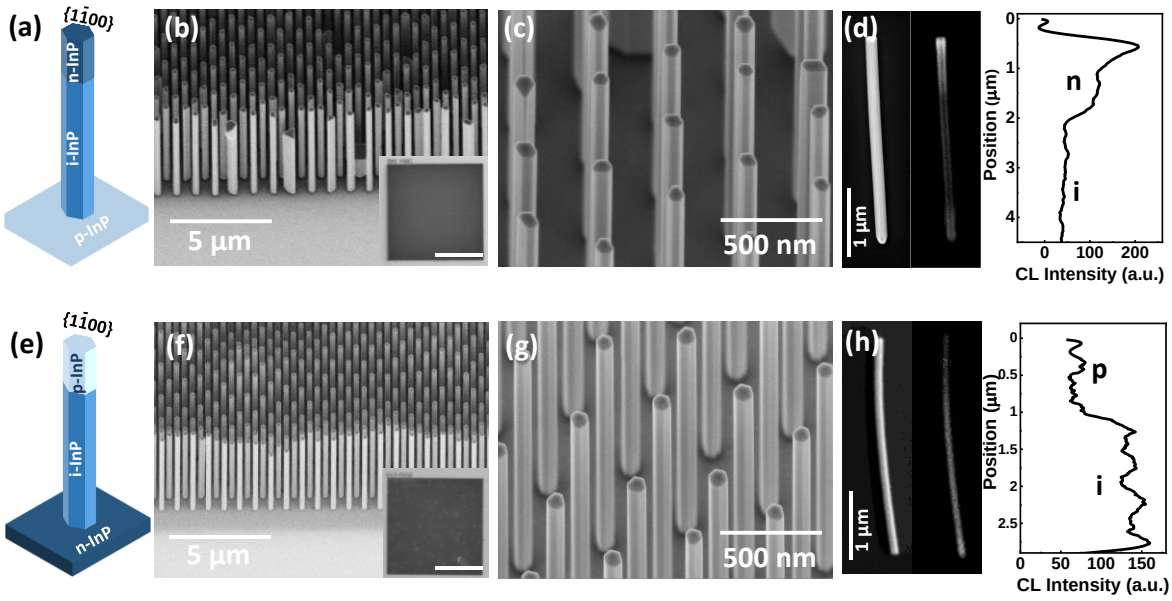

Figure 2. (a, b, c) Schematic and SEM images of i-n InP NW on p-doped InP substrate (p-i-n). (e, f, g) Schematic and SEM images of i-p InP NW on n-doped InP substrate (n-i-p). (d, h) SEM and corresponding cathodoluminescence (CL) image with CL spectrum intensity profile of p-i-n and n-i-p InP NW, respectively.

The doping profiles of the two NW structures were characterized by cathodoluminescence (CL) of single NWs,[25] transferred from NW arrays to a Si substrate, as shown in Figure 2d, h, clearly indicating the two different doping segments within these two structures. The bright-and-dark contrast of the CL panchromatic image[36] arises from different doping type and level of NW along the axial direction. Figure 2d shows that the n-segment has a much stronger luminescence than the i-segment, due to higher electron concentration, which increases transition probability of donor-valence band transition, in comparison to intrinsic-valence band transition. While for the p-doped top segment (Figure 2f), the transition probability of acceptor-valence band transition is lower than that of intrinsic-valence band transition, leading to a lower luminescence

in the p-segment than that in the i-segment. The SEM-CL characterization indicates that both n-i-p and p-i-n structures grown by SA-MOVPE method present well-defined junctions. The optical property of NWs was also assessed by PL and TRPL measurements (Figure S4 in SI), confirming good material quality.

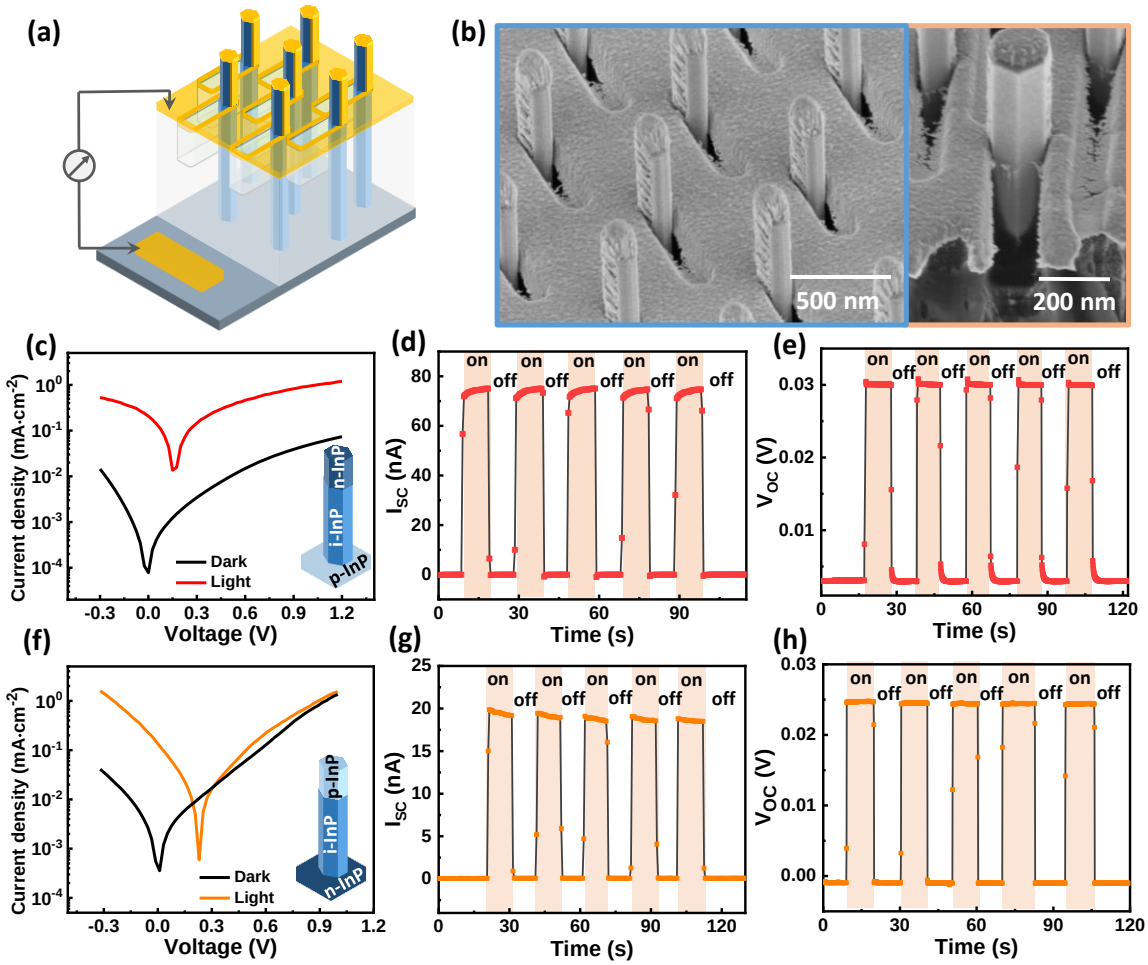

Figure 3. (a) Schematic of as-fabricated InP NW array sensor. (b) SEM image from the top of device, with a cross-sectional view highlighting the window at the top junction region opened for gas sensing (right panel). (c, f) Dark/light I−V characteristics of the p-i-n and n-i-p InP NW arrays (light source: solar simulator @AM1.5, 42.3 mW·cm^{-2}). (d, g) Time-dependent short-circuit current (I_{SC}) of p-i-n and n-i-p InP NW device, respectively; 'on' and 'off' correspond to states with and without illumination. (e, h) Time-dependent open-circuit voltage (V_{OC}) of p-i-n and n-i-p InP NW device, respectively.

For photovoltaic and sensing characterization, the as-grown NW arrays were then fabricated into an innovative NW PV sensor structure as illustrated in **Figure 3**a, by planarization (with polymer SU8-5), tilt-angle metal contact deposition[30] and gas exposure window opening steps

(detailed in SI section 2.3 and Figure S5). It is worth noting that based on the insight from our simulation, the length of the window structure is critical for high sensing performance. A long exposed i-region will maximise the NW surface interaction with the target gas molecules and thus the sensing response. Figure 3b presents the SEM images of a fabricated sensor, showing that this novel design has been successfully achieved with the top NW side wall partially covered with metal for electrical contact and exposed the other part in air for gas sensing. The electrical property of two NW device structures (p-i-n and n-i-p) was characterized by standard dark/light current-voltage (*I-V*) measurement as shown in Figure 3c, f. The dark *I-V* curves of both devices show typical diode characteristic. When illuminated under solar simulator @AM1.5 at a power of 42.3 $mW \cdot cm^{-2}$, both devices show PV behaviour, indicating successful device fabrication. The p-i-n and n-i-p structures have a I_{SC} density of 0.19 and 0.13 $mA \cdot cm^{-2}$ (device area of 200 × 200 μm^2), and an open-circuit voltage (V_{OC}) of 0.16 and 0.25 V, respectively. The time-dependent photo-responses are shown in Figure 3d, g and Figure 3e, h for I_{SC} and V_{OC}, where distinct 'ON' and 'OFF' PV states can be well manipulated to fit into the subsequent self-powered gas sensing measurements.

2.3 Laboratory Self-Powered Gas Sensing Performance

Sensing performance was characterized by detecting NO_2 in a gas sensing setup schematically illustrated in **Figure 4**a. The gas sensing chamber was configured to be illuminated by a solar simulator (with conditions equivalent to where the light I-V characteristics were measured) at zero bias, in order to characterize self-powered sensing performance. Prior to gas injection, the device was placed in the gas sensing chamber with illumination and constant air flow to generate steady-state I_{SC}. As NO_2 gas injection started, I_{SC} either decreased or increased, depending on the device structure as discussed earlier, and reached a saturation state in ~ 200 s (Figure S6a, 7a, SI). When NO_2 gas was switched off and air flow was resumed, I_{SC} recovered back to initial base level. Utilizing the variation of I_{SC} as a sensing signal, the NO_2 sensing *R* is then calculated according to Equation 1.

To find out the threshold light intensity for our self-powered NW sensor operation and the capacity of the device working under various illumination conditions, the p-i-n device was measured under a series of attenuated light intensity tuned by a neutral density filter. Figure 4b shows that with 100 ppb NO_2, the *R* value is consistent within the standard deviation range of *R* (22 ± 4.9 %) under a series of decreased light intensity from original level 42.3 $mW \cdot cm^{-2}$ (shaded area), even when the light intensity was decreased to 10% of its original level (or <5%

1sun condition). Under the reduced light intensity, the baseline I_{SC} (i.e., I_0) and the gas adsorption induced I_{SC} (i.e., I_{gas}) decreases simultaneously, such that the R calculated by Equation 1 remains at a similar value. Such light-intensity independent performance is highly desirable for sensing in realistic environment, since atmosphere solar irradiation usually varies drastically during a day.

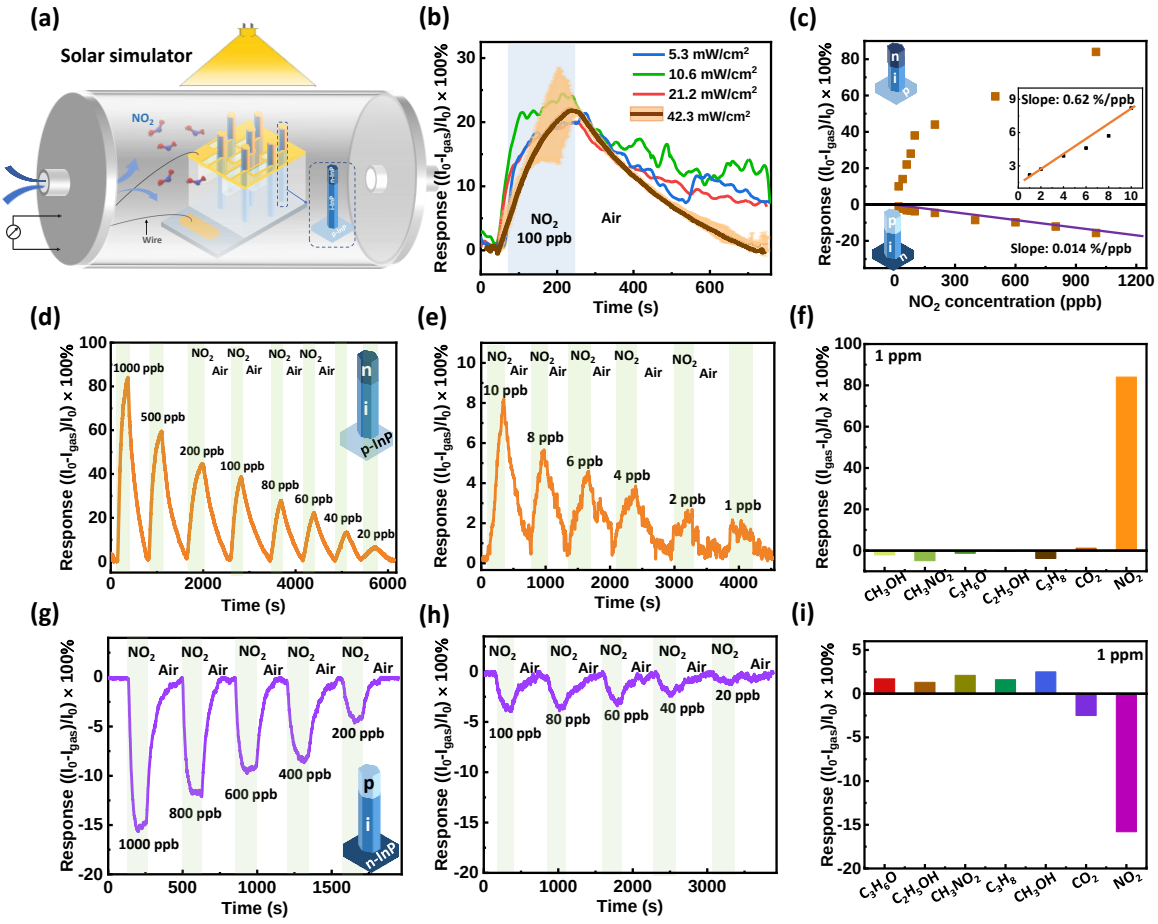

Figure 4. (a) Schematic of self-powered sensing measurement setup under illumination of solar simulator @AM1.5. (b) Time-dependent response measured from a p-i-n device under different illumination intensities. The averaged time-dependent sensing response and standard deviation range under light intensity 42.3 mW·cm^{-2} is shown as the shaded area. (c) Summarized NO_2 concentration vs. calculated response for p-i-n (upper panel) and n-i-p (lower panel) NW structures. The inset shows an enlarged graph of p-i-n sensing responses to 1-10 ppb NO_2. Sensing response measured from (d, e) p-i-n, and (g, h) n-i-p NW structures for different range of NO_2 concentrations. (f, i) Target gas selectivity measurement of p-i-n (f) and n-i-p (i) NW structures, respectively, with gas concentration of 1 ppm for methanol, methyl nitrides, acetone, ethanol, propane, CO_2, NO_2.

Figure 4d, e shows the time-dependent response of the p-i-n based device in concentration range 1 - 1000 ppb, and the n-i-p sample result is illustrated in Figure 4g, h, with concentration 20 - 1000 ppb. Figure 4c summarizes the corresponding concentration-dependent sensing response for both p-i-n and n-i-p sample with their linear-fitting slope (L) which is defined as device sensitivity, marking the sensor output signal changes with unit analytes input. It is noticeable that the absolute value of response at 1000 ppb and the device sensitivity for n-i-p structure (15.9 %, 0.014 %/ppb) is much smaller than p-i-n structure (84.1 %, 0.62 %/ppb), essentially verifying the results of numerical simulation that the NW with unipolar junction structure is superior to the bipolar one. According to aforementioned sensing mechanism in section 2.1, I_{SC} of n-i-p structure increases with NO_2 injected, thus giving negative sensing response, in contrast to the decreasing I_{SC} and positive sensing response from p-i-n structure (Figure S7a).[39-40] The responses from top p- and i-segment of the bipolar n-i-p junction structure offset each other, leading to a much-weakened sensing response. While, the combined sensing response from top n- and i-segment in p-i-n structure is additive, resulting in superior performance. For the more sensitive p-i-n structure, a linear correlation of response versus concentration can be clearly observed at two concentration regimes separately, with a smaller slope at the high concentration range (>100 ppb). This phenomenon also exists previously reported work, indicating that the sensor tended to saturate gradually due to the limitation of surface adsorption sites.[22, 37] On the other hand, the superior sensitivity performance of p-i-n structure is also indicated from the measurement of extremely low NO_2 concentration (1 ppb), where a distinguishable sensing response of 2% can still be obtained as shown in Figure 4e. Based on the classification of International Union of Pure and Applied Chemistry,[38] LOD is defined as three times of the standard deviation of sensing noise (S^2_{noise}), i.e. LOD = $3\times(S^2_{noise}/L)$. The calculated theoretical LOD obtained in this work is exceedingly small, ~ 0.49 ppb, with L = 0.62%/ppb, which is the lowest record achieved by self-powered gas sensor to the best of our knowledge.

To investigate the device reproducibility, the better performing p-i-n device was repeatedly exposed to NO_2 (at same concentration) and observed persistent sensing response for extended period of time (Figure S6c, d in SI). Furthermore, both of the n-i-p and p-i-n structure devices demonstrated a high selectivity to NO_2 as shown in Figure 4f, i. At 1 ppm level, the sensing response of these two devices to other organic vapours and common atmosphere gases (methanol (CH_3OH), ethanol (C_2H_5OH), methyl nitrite (CH_3NO_2), carbon dioxide (CO_2) and propane (C_3H_8)) are negligible comparing to NO_2. Besides I_{SC}, the time-dependent V_{OC} can be

also measured as an alternative readout signal that can be useful for integration with digital microchip circuit board, as demonstrated in Figure S6, S7 in SI.[34] The V_{OC} sensing response measured from both p-i-n and n-i-p NW sensors presents similar characteristics to what was observed with I_{SC}, i.e. the magnitude of sensing response is concentration dependent, and V_{OC} decreases (increases) similarly when exposed to NO_2 for p-i-n (n-i-p) structure.

Compared with different types of recently reported PV self-powered gas-sensing devices as summarized in **Table 1**, our p-i-n InP NW-based sensor shows an overall outstanding performance with high response (84% to 1 ppm NO_2), the lowest LOD (1 ppb), dual measurable signal (I_{SC} and V_{OC}) and ability to work stably under natural light source with different intensity other than certain wavelength or intensity.[41]

Table 1. Comparison of typical sensing performance parameters from self-powered gas sensors reported in the literature (room temperature operation).

Device structure	Light source	Measured signal	Target gas (LOD)	Response 100% (gas concentration)	Response/ recovery time (s)	Ref
p-i-n InP NW	Solar simulator (AM 1.5)	I_{SC} (nA) V_{OC} (mV)	NO_2 (1 ppb)	84% (1 ppm)	200 / 400	This work
p-Si/n-ZnO (amine-/thiol-functionalization)	Solar simulator (AM 1.5)	V_{OC} (mV)	NO_2 (170 ppb)	Amine: 7.5% Thiol: 9.8% (250 ppb)	~1000	[15]
CNT-SiNW	Solar simulator (AM 1.5)	V_{OC} (V)	NO_2 (10 ppm)	46% (10 ppm)	4-6	[17]
SWNTs/Si	λ = 600 nm, P = 1.8 mW cm^{-2}	V_{OC} (mV)	NO_2 (100 ppb)	2.23% (400 ppb)	~50	[42]
NiO/ZnO/ITO	Solar simulator 100 mW cm^{-2} AM1.5	V_{OC} (V)	CO_2	0.1%	150/100	[43]
$CsPbBr_3$	Solar simulator (AM 1.5)	I_{SC} (nA)	Acetone (1 ppm)	3% (1 ppm)	10/5	[16]
$CsPbBr_2I$	Solar simulator (AM 1.5)	I_{SC} (nA)	Acetone (1 ppm)	16% (1 ppm)	150	[44]
Gr/WS_2/Gr	White light P = 100 mW cm^{-2}	I_{SC} (μA) or V_{OC} (mV)	NO_2 (5ppm), H_2 (50ppm)	NO_2: 70% (5ppm), H_2: 17% (50ppm)	~500	[14]
SiNWs/ITO	Red LED λ = 576 nm, P = 20 mW cm^{-2}	I_{SC} (μA)	NO_2 (5ppb)	90% (1 ppm)	80/850	[41]
Au@rGO/GaN nanorods	UV LED λ = 382 nm, P = 1.71 mW cm^{-2}	I_{SC} (μA)	CO (5 ppm)	38% (20 ppm)	400/1000	[45]
FMCPIB	Solar simulator (AM 1.5)	I_{SC} (nA)	NO_2 (1 ppm)	8% (8 ppm)	17/126	[46]

2.4 On-Field Gas Sensing

Based on the laboratory sensing measurement results, the p-i-n NW sensor was chosen to confirm its applicability in a realistic environment. A real-time on-field measurement was enabled by connecting our NW device to a portable microprocessor with USB interface (JLM Innovation with supplementary software JLMlogSP), where electrical signal generated by the NW sensor is transmitted and processed. A prototype workflow from on-field sensing measurement to data analysis and output result is illustrated in **Figure 5**. Prior to on-field operation, a sensor calibration in self-powering mode was demonstrated, as shown in Figure 5a, which correlates sensing response value with NO_2 concentration. This calibration was performed in a laboratory gas sensing setup where the injected gas concentration was known and can be precisely controlled (detailed in SI, section 2.4 and Figure S8). However, when the NW sensor was connected to portable USB microprocessor, it could no longer be fitted into the same sensing setup. In this case, the calibration was then performed in a home-made 3D-printing enclosure (with an LED light source) that can accommodate the NW sensor integrated on the USB system (Figure S8). In this case, the enclosure was not as completely sealed and isolated from ambient atmosphere as in the standard gas sensing chamber. Hence, the measured sensing response tends to overestimate the injected gas concentration (i.e. considering certain amount of gas leakage). The calibration performed with the portable USB microprocessor locates the boundary of such overestimation. Therefore, it is expected that a real measurement result from vehicle exhaust should fall in between the two calibration lines as indicated by the pink shaded area.

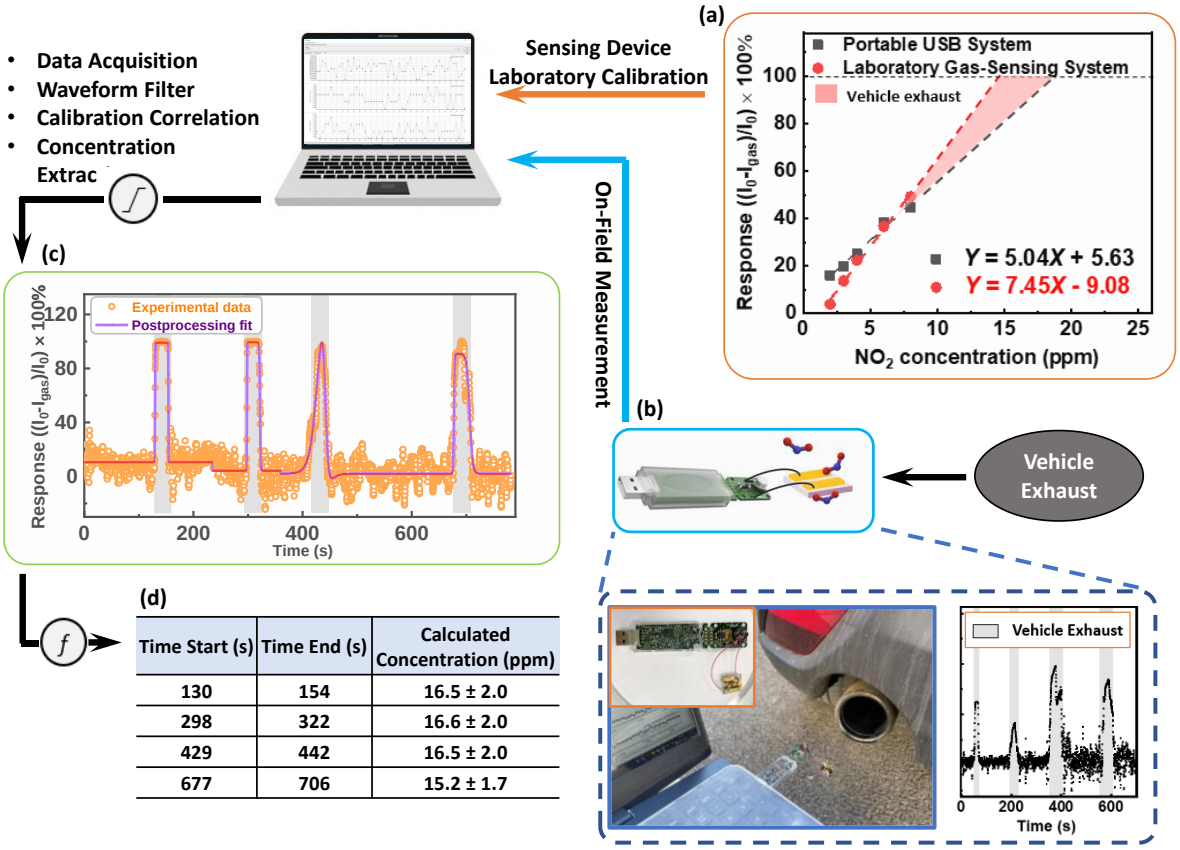

Time Start (s)	Time End (s)	Calculated Concentration (ppm)
130	154	16.5 ± 2.0
298	322	16.6 ± 2.0
429	442	16.5 ± 2.0
677	706	15.2 ± 1.7

Figure 5. A prototype workflow for practical on-field gas sensing measurement. (a) The NW sensor concentration calibration in laboratory environment (portable USB microprocessor system and laboratory gas sensing system). (b) The schematic and on-site photos of on-field vehicle exhaust measurement based on the NW sensor integrated with the USB interface and an example of acquired data. (c) Data measured by this USB interface and the corresponding post-processed fitting result by user-specified data filters to remove noise and extract sensing response values; (d) By correlating with the laboratory calibration, the NO_2 concentration can dynamically monitored.

The portable NW sensor system was then brought to the realistic environment for on-field measurement with the exposure of a 4-cylinder gasoline car exhaust (Figure 5b). An example time-dependent response curve shows that the value and shape of response pulse vary in different accelerator pedal pressing duration and revolutions per minute (RPM) of the engine, as NO_2 concentration in exhaust gas depending on these parameters. The measured response curve, together with the calibration results, was transmitted to a data evaluation unit (e.g., a laptop, or an embedded system with USB or Bluetooth interface) for processing. Here we demonstrate a simple pipeline of data acquisition and processing (Figure 5c) for a vehicle exhaust at 2500 RPM where the gas pedal was pressed four times, each of which lasted

approximately 25 s. The raw data from the measurement was then evaluated with a logistic filter to remove noise (e.g. a double-logistic filter in this demonstration) to extract sensing response value. The NO_2 concentration was then calculated based on the calibration curves. The whole pipeline can be easily integrated in a Python script to interact with this portable USB interface. The calculated NO_2 average concentration is ~15.46 ppm, in good agreement with previously reported gasoline-powered motor vehicle NO_2 emission study,[47-48] indicating the practical functionality and accuracy of our NW sensor system.

To improve the device performance and functionalities, the p-i-n structure can be further optimized by reducing n-segment length and increasing i-segment length to further improve the sensitivity. Apart from the axial p-n junction, it may be worth investigating a radial-junction p-n NW structure, which could not only provide a larger junction region but also simplify the device fabrication process. Furthermore, multiple NW arrays with varied pitch sizes and diameters can be grown during the same epitaxial growth sequence to provide multi-channel detection, which could enhance the dynamic range of the NO_2 detection.

3. Conclusion

In this work, a novel self-powered sensor architecture is successfully designed and demonstrated based on bottom-up grown p-n homojunction InP NW arrays. We designed the p-n junction-based NW sensor structure and explored the sensing mechanism via numerical simulation. The fabricated sensors based on this p-n junction InP NW array show excellent sensitivity with a limit of detection down to sub-ppb level and high selectivity to NO_2 in self-powered operation mode. These results promise a new family of self-powered sensing platform to achieve high-performance gas sensor with a strong enviroment fidelity enabled by photovoltaic effect. The integration of the NW sensor with a portable USB interface for practical dynamic on-field measurement is further demonstrated, precisely quantifying NO_2 concentration from a motor vehicle exhaust. Our prototype InP NW sensor design paves a way towards battery-free, highly integrable and compatible sensing platform for applications such as environmental monitoring, industrial safety and hazard alarming. It is a promising step forward to the next-generation sensing network for Internet of Things.

Supporting Information

Supporting Information is available from the Wiley Online Library or from the author.

Acknowledgements

The authors acknowledge the financial support from the Australian Research Council. The authors also acknowledge the Australian National Fabrication Facility (ACT node) for facility support. This research was also funded by and has been delivered in partnership with Our Health in Our Hands (OHIOH), a strategic initiative of the Australian National University, which aims to transform healthcare by developing new personalized health technologies and solutions in collaboration with patients, clinicians, and health care providers. A.T. gratefully acknowledges the support of the Australian Research Council for a Future Fellowship (FT200100939) and Discovery grant DP190101864. A.T. also acknowledges financial support from the North Atlantic Treaty Organization Science for Peace and Security Programme project AMOXES (#G5634). S.W. thanks the China Scholarship Council and the Australian National University for scholarship support.

Received:

Revised:

Published online:

References

[1] Z. Y. Qian, S. H. Kang, V. Rajaram, C. Cassella, N. E. McGruer and M. Rinaldi, *Nat. Nanotechnol.* **2017**, *12*, 969-973.

[2] M. Shirvanimoghaddam, K. Shirvanimoghaddam, M. M. Abolhasani, M. Farhangi, V. Z. Barsari, H. Y. Liu, M. Dohler and M. Naebe, *Ieee Access* **2019**, *7*, 94533-94556.

[3] X. Li, C. Q. Luo, H. Ji, Y. D. Zhuang, H. L. Zhang and V. C. M. Leung, *Int. J. Commun. Syst.* **2020**, *33*, 4171.

[4] A. Ahmed, I. Hassan, M. F. El-Kady, A. Radhi, C. K. Jeong, P. R. Selvaganapathy, J. Zu, S. Ren, Q. Wang and R. B. Kaner, *Adv. Sci.* **2019**, *6*, 2925.

[5] V. A. Aksyuk, *Nat. Nanotechnol.* **2017**, *12*, 939-940.

[6] H. Askari, E. Hashemi, A. Khajepour, M. B. Khamesee and Z. L. Wang, *Nano Energy* **2018**, *53*, 1003-1019.

[7] Z. Y. Wu, T. H. Cheng and Z. L. Wang, *Sensors* **2020**, *20*, 2925.

[8] Z. L. Song, W. H. Ye, Z. Chen, Z. S. Chen, M. T. Li, W. Y. Tang, C. Wang, Z. A. Wan, S. Poddar, X. L. Wen, X. F. Pan, Y. J. Lin, Q. F. Zhou and Z. Y. Fan, *Acs Nano* **2021**, *15*, 7659-7667.

[9] E. Lee and H. Yoo, *Molecules* **2021**, *26*, 1802230.

[10] Z. Wen, Q. Q. Shen and X. H. Sun, *Nanomicro Lett.* **2017**, *9*, 45.

[11] X. L. Liu, Y. Zhao, W. J. Wang, S. X. Ma, X. J. Ning, L. Zhao and J. Zhuang, *IEEE Sens. J.* **2021**, *21*, 5628-5644.

[12] P. A. Laplante, M. Kassab, N. L. Laplante and J. M. Voas, *IEEE Intell. Syst.* **2018**, *12*, 3030-3037.

[13] Y. Kim, S. Lee, J.-G. Song, K. Y. Ko, W. J. Woo, S. W. Lee, M. Park, H. Lee, Z. Lee, H. Choi, W.-H. Kim, J. Park and H. Kim, *Adv. Funct. Mater.* **2020**, *30*, 2003360.

[14] D. Lee, H. Park, S. D. Han, S. H. Kim, W. Huh, J. Y. Lee, Y. S. Kim, M. J. Park, W. I. Park, C.-Y. Kang and C.-H. Lee, *Small* **2019**, *15*, 1804303.

[15] M. W. G. Hoffmann, L. Mayrhofer, O. Casals, L. Caccamo, F. Hernandez-Ramirez, G. Lilienkamp, W. Daum, M. Moseler, A. Waag, H. Shen and J. D. Prades, *Adv. Mater.* **2014**, *26*, 8017-8022.

[16] H. Chen, M. Zhang, R. Bo, C. Barugkin, J. Zheng, Q. Ma, S. Huang, A. W. Y. Ho-Baillie, K. R. Catchpole and A. Tricoli, *Small* **2018**, *14*, 1702571.

[17] Y. Jia, Z. Zhang, L. Xiao and R. Lv, *Nanoscale Res. Lett.* **2016**, *11*, 299.

[18] X. L. Liu, S. X. Ma, S. W. Zhu, Y. Zhao, X. J. Ning, L. Zhao and J. Zhuang, *Sens. Actuators B Chem.* **2019**, *291*, 345-353.

[19] X. L. Liu, Y. Zhao, S. X. Ma, S. W. Zhu, X. J. Ning, L. Zhao and J. Zhuang, *Acs Sensors* **2019**, *4*, 3056-3065.

[20] M. W. G. Hoffmann, O. Casals, A. E. Gad, L. Mayrhofer, C. Fabrega, L. Caccamo, F. Hernandez-Ramirez, G. Lilienkamp, W. Daum, M. Moseler, H. Shen, A. Waag and J. D. Prades, in *Eurosensors 2015*, (Eds: G. Urban, J. Wollenstein and J. Kieninger) **2015**, p. 623-627.

[21] E. Modaresinezhad and S. Darbari, *Sens. Actuators B Chem.* **2016**, *237*, 358-366.

[22] X.-L. Liu, Y. Zhao, S.-X. Ma, S.-W. Zhu, X.-J. Ning, L. Zhao and J. Zhuang, *ACS Sensors* **2019**, *4*, 3056-3065.

[23] M. A. Green, E. D. Dunlop, J. Hohl-Ebinger, M. Yoshita, N. Kopidakis, K. Bothe, D. Hinken, M. Rauer and X. Hao, *Prog. Photovolt.: Res. Appl.* **2022**, *30*, 687-701.

[24] Q. Gao, Z. Li, L. Li, K. Vora, Z. Li, A. Alabadla, F. Wang, Y. Guo, K. Peng, Y. C. Wenas, S. Mokkapati, F. Karouta, H. H. Tan, C. Jagadish and L. Fu, *Prog. Photovolt.: Res. Appl.* **2019**, *27*, 237-244.

[25] Z. Y. Li, I. Yang, L. Li, Q. Gao, J. S. Chong, Z. Li, M. N. Lockrey, H. H. Tan, C. Jagadish and L. Fu, *Prog. Nat. Sci.: Mater. Int.* **2018**, *28*, 178-182.

[26] W. N. Du, X. G. Yang, H. Y. Pan, X. H. Ji, H. M. Ji, S. Luo, X. W. Zhang, Z. G. Wang and T. Yang, *Nano Lett.* **2016**, *16*, 877-882.

[27] J. C. Shin, K. H. Kim, K. J. Yu, H. F. Hu, L. J. Yin, C. Z. Ning, J. A. Rogers, J. M. Zuo and X. L. Li, *Nano Lett.* **2011**, *11*, 4831-4838.

[28] R. Janissen, P. K. Sahoo, C. A. Santos, A. M. da Silva, A. A. G. von Zuben, D. E. P. Souto, A. D. T. Costa, P. Celedon, N. I. T. Zanchin, D. B. Almeida, D. S. Oliveira, L. T. Kubota, C. L. Cesar, A. P. de Souza and M. A. Cotta, *Nano Lett.* **2017**, *17*, 5938-5949.

[29] J. H. Yu, M. K. Xu, L. Y. Liang, M. Guan, Y. Zhang, F. Yan and H. T. Cao, *Appl. Phys. Lett.* **2020**, *116*, 4.

[30] S. Wei, Z. Li, A. John, B. I. Karawdeniya, Z. Li, F. Zhang, K. Vora, H. H. Tan, C. Jagadish, K. Murugappan, A. Tricoli and L. Fu, *Adv. Funct. Mater.* **2022**, *32*, 2107596.

[31] Q. Gao, D. Saxena, F. Wang, L. Fu, S. Mokkapati, Y. A. Guo, L. Li, J. Wong-Leung, P. Caroff, H. H. Tan and C. Jagadish, *Nano Lett.* **2014**, *14*, 5206-5211.

[32] S. Y. Wei, Z. Li, A. John, B. I. Karawdeniya, Z. Y. Li, F. L. Zhang, K. Vora, H. H. Tan, C. Jagadish, K. Murugappan, A. Tricoli and L. Fu, *Adv. Funct. Mater.* **2022**, *32*, 2107596.

[33] Q. Gao, Z. Y. Li, L. Li, K. Vora, Z. Li, A. Alabadla, F. Wang, Y. A. Guo, K. Peng, Y. C. Wenas, S. Mokkapati, F. Karouta, H. H. Tan, C. Jagadish and L. Fu, *Prog Photovolt.* **2019**, *27*, 237-244.

[34] Y. Kim, S. Lee, J. G. Song, K. Y. Ko, W. J. Woo, S. W. Lee, M. Park, H. Lee, Z. Lee, H. Choi, W. H. Kim, J. Park and H. Kim, *Adv. Funct. Mater.* **2020**, *30*, 2003360.

[35] M. Bai, H. Huang, Z. Liu, T. T. Zhan, S. F. Xia, X. G. Li, N. Sibirev, A. Bouravleuv, V. G. Dubrovskii and G. Cirlin, *Appl. Surf. Sci.* **2019**, *498*, 143756.

[36] I. Yang, X. Zhang, C. L. Zheng, Q. Gao, Z. Y. Li, L. Li, M. N. Lockrey, H. Nguyen, P. Caroff, J. Etheridge, H. H. Tan, C. Jagadish, J. Wong-Leung and L. Fu, *Acs Nano* **2018**, *12*, 10374-10382.

[37] X. Zhou, J. Y. Liu, C. Wang, P. Sun, X. L. Hu, X. W. Li, K. Shimanoe, N. Yamazoe and G. Y. Lu, *Sens. Actuators B Chem.* **2015**, *206*, 577-583.

[38] T. Pham, G. Li, E. Bekyarova, M. E. Itkis and A. Mulchandani, *ACS Nano* **2019**, *13*, 3196-3205.

[39] D. Lynall, A. C. Tseng, S. V. Nair, I. G. Savelyev, M. Blumin, S. L. Wang, Z. M. M. Wang and H. E. Ruda, *Acs Nano* **2020**, *14*, 964-973.

[40] H. Long, A. Harley-Trochimczyk, T. Pham, Z. R. Tang, T. L. Shi, A. Zettl, C. Carraro, M. A. Worsley and R. Maboudian, *Adv. Funct. Mater.* **2016**, *26*, 5158-5165.

[41] D. Liu, Q. Chen, A. Chen and J. Wu, *RSC Adv.* **2019**, *9*, 23554-23559.

[42] L. Liu, G. H. Li, Y. Wang, Y. Y. Wang, T. Li, T. Zhang and S. J. Qin, *Nanoscale* **2017**, *9*, 18579-18583.

[43] T. Hamada and M. Sugiyama, *Jpn J Appl Phys* **2022**, *61*, 054002.

[44] H. Chen, M. Zhang, X. Fu, Z. Fusco, R. Bo, B. Xing, H. T. Nguyen, C. Barugkin, J. Zheng, C. F. J. Lau, S. Huang, A. W. Y. Ho-Baillie, K. R. Catchpole and A. Tricoli, *Phys. Chem. Chem. Phys*. **2019**, *21*, 24187-24193.

[45] M. Reddeppa, S. B. Mitta, T. Chandrakalavathi, B. G. Park, G. Murali, R. Jeyalakshmi, S. G. Kim, S. H. Park and M. D. Kim, *Curr. Appl. Phys.* **2019**, *19*, 938-945.

[46] H. Chen, M. Zhang, B. Xing, X. Fu, R. Bo, H. K. Mulmudi, S. Huang, A. W. Y. Ho-Baillie, K. R. Catchpole and A. Tricoli, *Adv. Opt. Mater.* **2020**, *8*, 1901863.

[47] G. A. Ban-Weiss, J. P. McLaughlin, R. A. Harley, A. J. Kean, E. Grosjean and D. Grosjean, *Environ. Sci. Technol.* **2008**, *42*, 3944-3950.

[48] G. Dooly, E. Lewis, C. Fitzpatrick and P. Chambers, *IEEE Sens. J.* **2007**, *7*, 685-691.

The table of contents

An innovative self-powered room-temperature nitrogen dioxide (NO_2) sensor is presented based on indium phosphide homojunction nanowire array. The proof-to-concept sensor structure has been demonstrated with high sensitivity, stability and selectivity. It is integrated to USB interface for on-field vehicle exhaust measurement. This work promises a new family of III-V compound semiconductor nanostructures self-powered sensor, for future mega-scale Internet-of-Things systems.

S. Wei, Z. Li, K. Murugappan, Z. Y. Li, F. Zhang, M. Lysevych, H. H. Tan, C. Jagadish, A. Tricoli, L. Fu

Self-Powered Portable Nanowire Array Gas Sensor for Dynamic NO_2 monitoring at room temperature

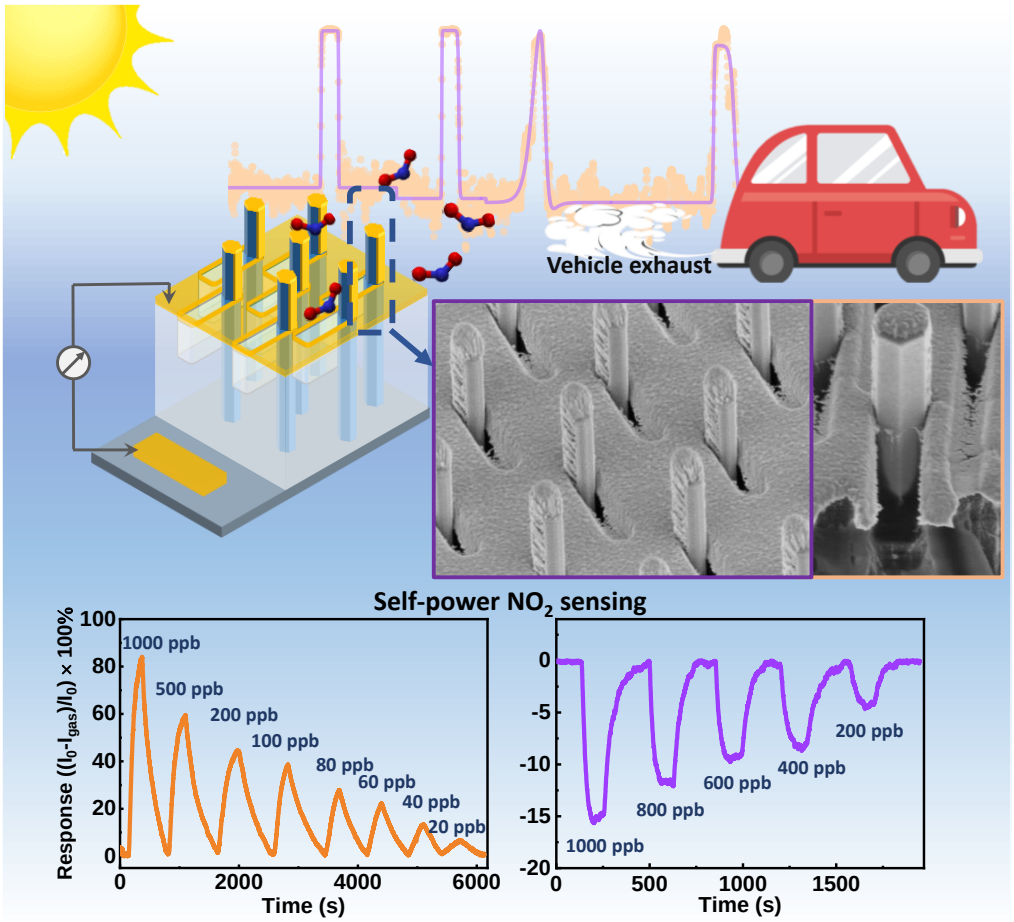

Supporting Information

Self-Powered Portable Nanowire Array Gas Sensor for Dynamic NO_2 monitoring at room temperature

Shiyu Wei, Zhe Li, Krishnan Murugappan, Ziyuan Li, Fanlu Zhang, Mykhaylo Lysevych, Hark Hoe Tan, Chennupati Jagadish, Antonio Tricoli*, and Lan Fu**

1. Numerical simulation

The gas sensing simulation was performed using the semiconductor module of COMSOL Multiphysics. To ensure timely convergence of simulated processes, only a 2D equivalent unit cell of nanowire (NW) array device, consisting of a single NW, was constructed in simulation. The 3D view, together with 2D simulation geometry of the unit cell is illustrated in Figure S1. The exposure window is fixed at 700 nm measured from the top of NWs, while the junction depth is varied from 350 nm to 1800 nm. The left surface within this window is subject to gas exposure, for which a negative surface charge boundary condition is applied to model oxidative NO_2 adsorption. The light generation is only enabled within the window, below which is considered negligible since light is largely blocked by metal contact (see Figure 1). The top horizontal boundary, together with right side boundary (300 nm from the top), is set as Ohmic contact to replicate realistic device structure. All simulation related parameters are summarized in Table S1.

Table S1 Material and Model Parameters in the Numerical Simulations

Material/Model Parameters	Value	Comments
Electron mobility	120 cm^2 ($V^{-1}s^{-1}$)	[1]
Hole mobility	100 cm^2 ($V^{-1}s^{-1}$)	[2]
SRH recombination lifetime	190 ps	Based on TRPL measurement; see Figure S4
Doping concentration top P-doped NW	1×10^{17} cm^{-3}	[2]
Doping concentration i-region	1×10^{16} cm^{-3}	[2]
Doping concentration top N-doped NW	3×10^{18} cm^{-3}	[2]

Doping concentration P-/N-doped substrate	1×10^{18} cm^{-3}	[2]
Top N-/P-doped NW segment thickness	Adjustable parameter	Varied from 350 nm to 1800 nm
i-region thickness	Adjustable parameter	Total thickness of top NW segment plus i-region is 3 μm; i-region thickness changes correspondingly.
InP nanowire radius	100 nm	

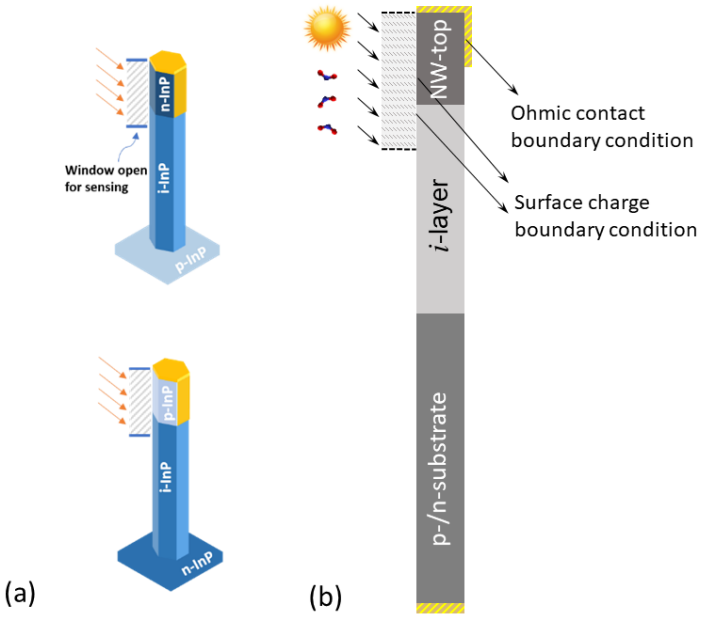

Figure S1. (a) Device schematics of p-i-n and n-i-p based NW array sensor. (b) Two-dimensional simulation domain deployed in COMSOL Multiphysics.

2. Experimental Section

2.1 p-i-n junction InP NW growth

1) Substrate processing

Figure S2 illustrates the processes of preparing InP (111)A substrate (both p-doped and n-doped with a concentration of (0.8-8) $\times 10^{18}$) NW growth. Firstly, a 30 nm SiO_2 layer was deposited on (111)A InP substrate by plasma enhanced chemical vapor deposition (PECVD) at 300 °C, and the thickness was measured by ellipsometry. A negative photoresist AR6200.09 was spin-coated (step 1: 500 rpm 5 s; step 2: 2000 rpm for 60 s) on SiO_2 layer and baked at 150°C for 1 min on hotplate. Then, the resist was exposed by a Raith 150 electron beam lithography (EBL) system based on a designed pattern consisting of 200 × 200 μm^2 hexagonal dot array with a size of 80 nm and pitch of 600 nm. The exposed pattern area in photoresist layer was removed by the corresponding resist developer. After the development of resist, oxygen plasma (RF

power: 300 W; 300 sccm O_2 flow; 2 min,) was used to remove the footage residues in the patterned area. The exposed pattern was then etched by RIE to remove the SiO_2 layer on InP substrate (RF power: 20W; 20 sccm CHF_3 flow; 4.5 min). To remove the possible damage on the exposed InP surface during SiO_2 deposition, 10% H_2O_2 was first used to oxidize the InP layer for 2 min followed by etching off the oxide layer with 10 % H_3PO_4 solution for 2 min. These steps were repeated sequentially for 5 times and then, the sample was immediately transferred into the metal-organic vapor-phase epitaxy (MOVPE) reactor for NW growth.

2) p-i-n InP NW growth

The InP NW arrays were grown with an AIXTRON 200/4 MOVPE reactor, operating at a base pressure of 100 mbar, using H_2 as a carrier gas with a total flow of 14.5 l/min. Trimethylindium (TMIn) and phosphine (PH_3) were used as precursors for the group III (In) and group V (P) elements, respectively. Molar fractions of TMIn and PH_3 were set at 9.38×10^{-6} and 7.59×10^{-4}, respectively, corresponding to a V/III ratio of 80. All samples were hot baked at 750 °C for 10 min under the PH_3 flow and grown for 4 min at 730 °C for undoped segment (i-InP). Then, Silane (SiH_4) and diethylzinc (DEZn) were introduced during the growth of n-doped segment and p-doped segment for 2 min with all the other parameters kept the same as those used for the growth of undoped InP segment. With this two-step growth process, the i-n and i-p InP NW were grown on p-doped and n-doped substrate respectively, to form n-i-p and p-i-n junctions.

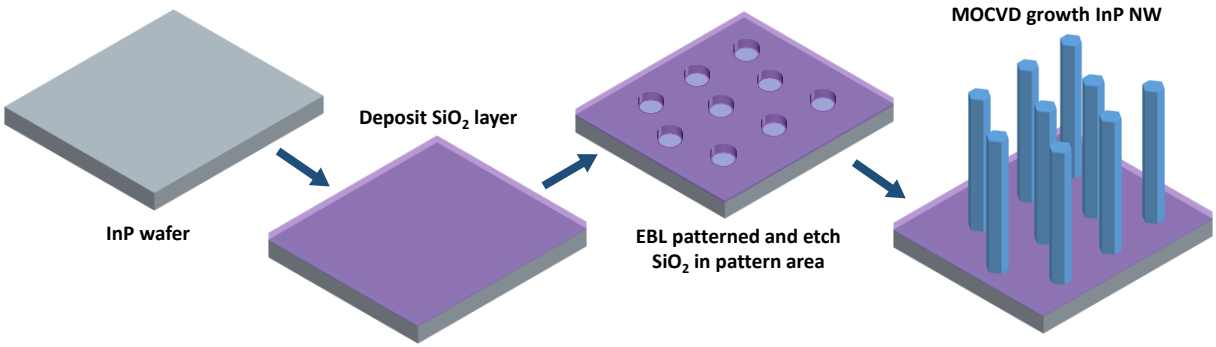

Figure S2. Schematic of NW growth process by selective-area metal-organic vapor-phase epitaxy (SA-MOVPE).

2.2 InP NW characterization

The morphology of the as-grown InP NW arrays were characterised by scanning electron microscopy (FEI VERIOS 460 SEM) with electron beam voltage of 2 kV and current of 13 pA. Cathodoluminescence (CL) technique was applied on single NWs which wwer transferred from

the array to a Si substrate to characterize its optical property. The CL images were acquired with SEM system equipped with a Gatan MONO CL4 components under an electron excitation voltage of 10 kV and current of 0.8 nA at room temperature. The crystal structure is determined by transmission electron microscopy (JEOL 2100F TEM) analysis of NWs that were directly transferred from original array to a copper mesh. Figure S3 presents the TEM images taken along {2110} zone axis from top and bottom region of a i-n NW confirming that NW was grown in wurtzite phase with barely any crystalline defects, and the dopants have negligible effect to the NW crystalline.

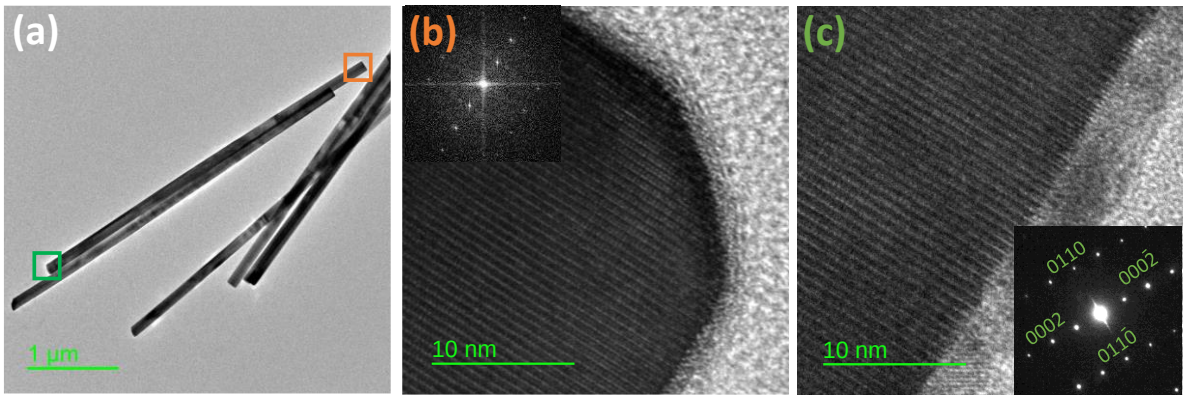

Figure S3. (a) Bright-field AC-STEM image shows the morphology of a typical i-n InP NW grown at 730 °C. (b, c) High-resolution TEM (HRTEM) images taken along [110] zone axis from the top and bottom regions of the InP NW shown in (a). Inset of (b) is the fast Fourier transform (FFT) image. Inset of (c) shows the selected area electron diffraction pattern confirming the WZ crystalline structure NW.

The NWs were also transferred to SiO_2/Si substrate for time-resolved photoluminescence (TRPL) measurement. PL spectra were acquired along single NW from top to bottom position (P1 to P3) at room temperature (Figure S4).[4] The TRPL system is composed of Horiba LabRAM system equipped with confocal optics, a diode pumped solid-state (DPSS) 532 nm laser, and a liquid nitrogen-cooled array InGaAs detector. The laser beam was focused through a 100x microscope objective lens, resulting in a spot size of 0.36 µm (in radius) estimated by vector diffraction calculation. The minority carrier lifetime in the NWs was extracted from the single exponential fitting of TRPL decay curve. The emission was collected by the same objective lens and detected by a single photon avalanche diode, which was connected to the Picoharp 300 time-correlated single photon counting (TCSPC) system.

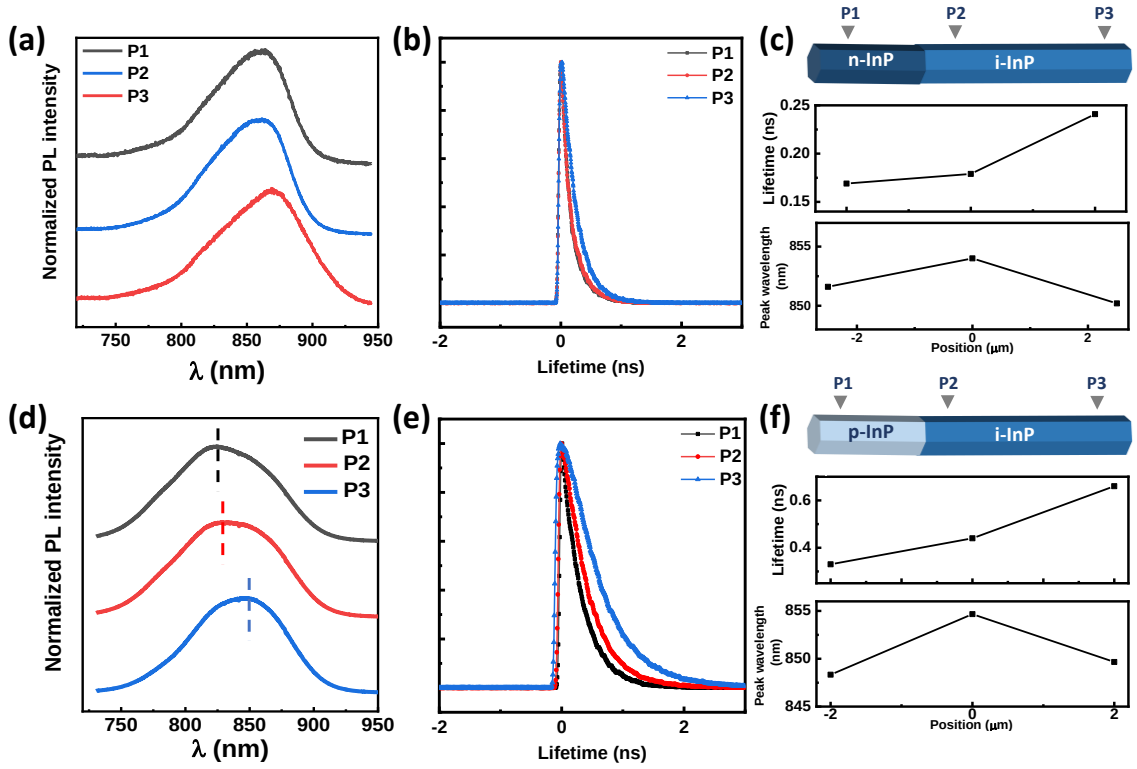

Figure S4. (a, d) Room-temperature photoluminescence (PL) spectra of n-i InP and p-i InP at top, middle and bottom, respectively. (b, e) Time-resolved PL (TRPL) decays measured at the peak emission wavelength of n-i InP and p-i InP at the same position. (c, f) Minority carrier lifetimes and peak wavelength extracted from TRPL measurement (a-d).

For i-n NW, the PL spectrum is similar at different locations of NW with peak wavelength around 853 nm and the lifetime extracted from the time-resolve PL (TRPL)[5] decay is ~0.15 ns for these three positions. While the peak wavelength of i-p NW shows an obvious blue shift at P1, its lifetime (~0.4 ns) is also shorter than P2 (~0.5 ns), P3 (~0.6 ns), which may be resulted from large Zn dopant interdiffusion during the growth of the p-segment. It is also noticeable that the lifetime of n-i-p is much larger than p-i-n, because top n-doping segment concentration (~3×10^{18} cm^{-3}) is higher than that of top p-doping segment (~1×10^{17} cm^{-3}).[6]

2.3 Fabrication process of self-powered InP axial junction NW NO_2 sensor

To fabricate a chemiresistive sensor based on InP axial junction NW array, photoresist SU8-5 (Kirsten Hackenbroich), was spin-coated on NW arrays to fully cover the whole vertical NW arrays. Then SU8-5 was etched back by barrel-etcher (PVA Tepla Gigabatch 310 M) with O_2 flow rate of 300 sccm and power of 500 W to expose ~500 nm of the top of InP NWs for subsequent electrical contact. Then the sample was flood exposed under UV illumination and

baked at 200 °C to solidify SU8-5. Since the top junction is deeper than 500 nm, the i-segment of NW is embedded in SU8-5, which prevents shorting of the junction and provides necessary mechanical support to the NWs.

A 200 nm Au layer was deposited on nanowires using e-beam evaporator for contacting. The samples were mounted on a special holder to enable the tile-angle deposition to provide not only electrical contact, but also partially exposed the nanowires to allow gas adsorption and sensing.[3] The tilt-angle deposition leaves a shadow area behind each NW covered by SU8-5, which can be further etched to extend the exposure window further below the top junction. The etching rate of Inductively Coupled Plasma (ICP) etching has been well calibrated such that another ~500 nm of SU8-5 was removed precisely as shown in **Figure S5c**. The SU8-5 layer shadowed by NW during deposition was exposed and subsequently etched by ICP-F, which formed a hole besides each NW. Then, a 200 nm Au layer was deposited on the InP substrate as bottom contact. The fabricated chemiresistive sensors were characterized for their sensing performance.

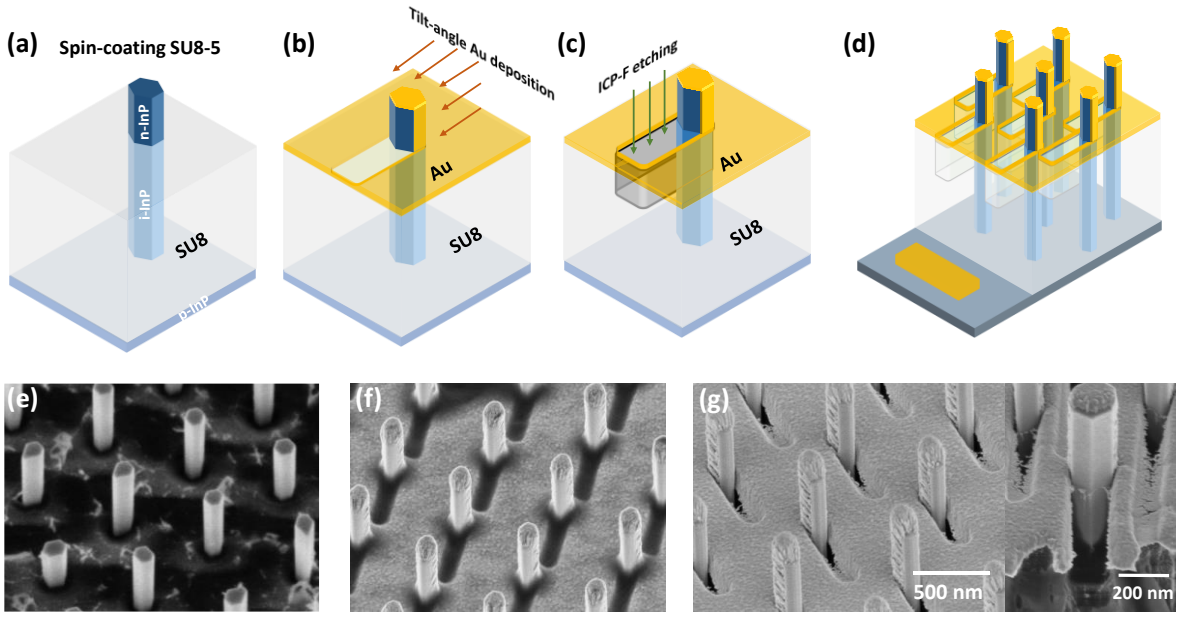

Figure S5. (a-c) Schematic of device fabrication process based on as-grown InP NWs including (a) spin-coating of SU8-5, (b) tilt-angle deposition of Au, and (c) ICP-F etching. (d-f) SEM images corresponding to the fabrication process (a-c).

2.4 Electrical characterization

The electrical and photovoltaic (PV) property of InP nanowire array was characterized by current-voltage (I−V) curve by a Keysight system B2902A source/measurement unit, incorporated with solar simulator.

2.5 NO_2 sensing measurement

The gas sensing performance was measured by home-made sensing setup which consists of a Linkam chamber with a sample stage and Au probes for electrical contacting, mass flow controllers (MFCs Bronkhorst), a solar simulator and gas cylinders. For any gas sensing measurements, the carrier gas was simulated air with volume ratio of N_2 to O_2 at 4 (V_{N2}/V_{O2} = 4, N_2 and O_2, BOC gas). The gas flow rate was controlled by MFCs while the total gas flow rate was kept at 1 l/min for ppm level concentration test and 0.5 l/min for sub-ppm level concentration test. For the measurement of analyte gas, volatile organic compounds (VOCs) (ethanol, 9.91 ppm in N_2, Coregas; acetone, 10.1 ppm in N_2, Coregas; methanol, 10 ppm in N_2, BOC gas) or NO_2 gas was diluted to desired concentration before being purged into the chamber.

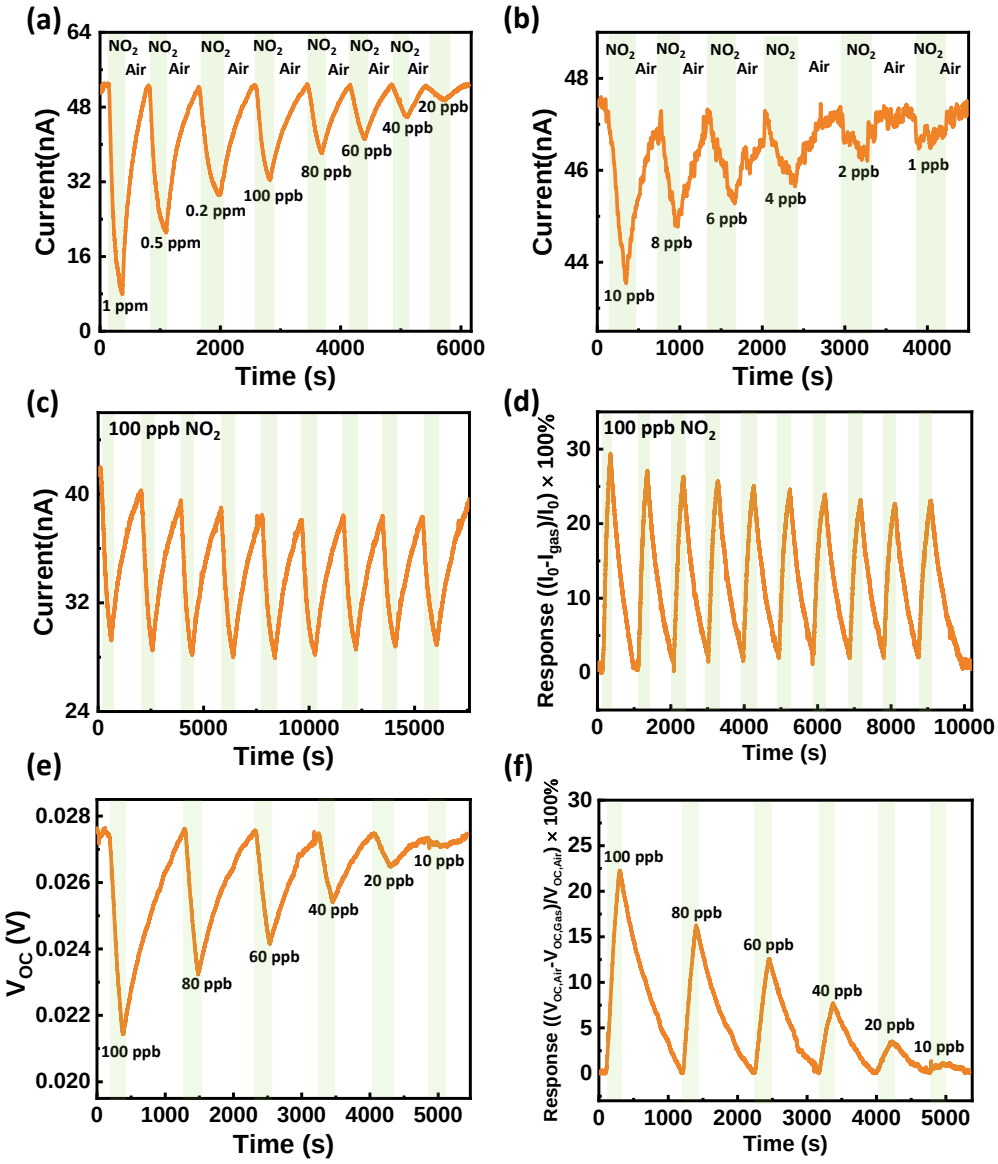

Figure S6. Raw data from p-i-n InP NW photocurrent sensing measurement with concentration ranging from (a) 20-1000 ppb, (b) 1-10 ppb, and repeated sensing measurement with 100 ppb NO_2 (c). These three figures correspond to Figure 4b, 4c, 4e in the main text, respectively. (e) Repeated sensing measurement with 100 ppb NO_2. (e-h) V_{OC} as output signal for NO_2 sensing measurement and the corresponding calculated response with p-i-n sample (e, f) and n-i-p (g, h) samples.

The V_{OC} of the p-i-n NW sensor decreases with the NO_2 exposure which is concentration dependent like I_{SC}. The sensing performance is slightly inferior to the I_{SC} sensing result that the response of 100 ppb NO_2 is around 22.5% and LOD is 10 ppb. When exposed to NO_2, V_{OC} decreases for p-i-n structure and increases for n-i-p structure, giving either positive or negative sensing response, which is consistent with those measured from I_{SC}. The open-circuit condition

corresponds to where dark current completely cancels PV current. For p-i-n structure where majority carriers are diminished due to gas exposure, it needs a smaller PV voltage for such cancellation to happen (thus a decreased V_{OC} when in contact with gas); whereas for n-i-p structure, majority carrier enhancement also boosts dark current and hence requires a larger voltage for open-circuit condition to happen (i.e. an increased V_{OC} when exposed to gas).

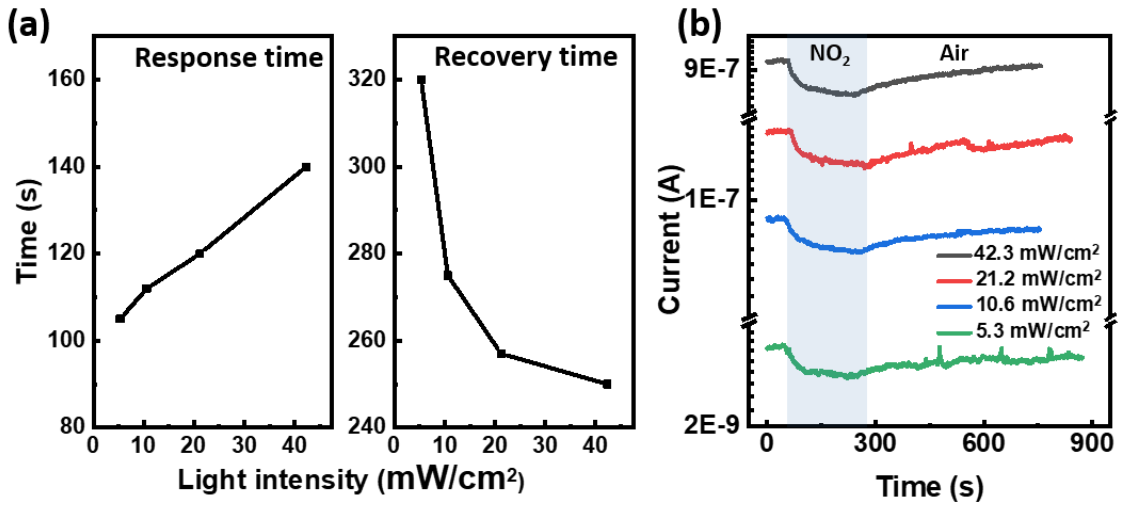

Figure S7. (a) NO_2 sensing response and recovery time of p-i-n InP nanowire sensor under the light intensity from 5.3 to 42.3 $mW \cdot cm^{-2}$. (b) Raw data of photocurrent from the sensing measurement based on the p-i-n sensor exposed to 100 ppb under the same varying light intensities as (a).

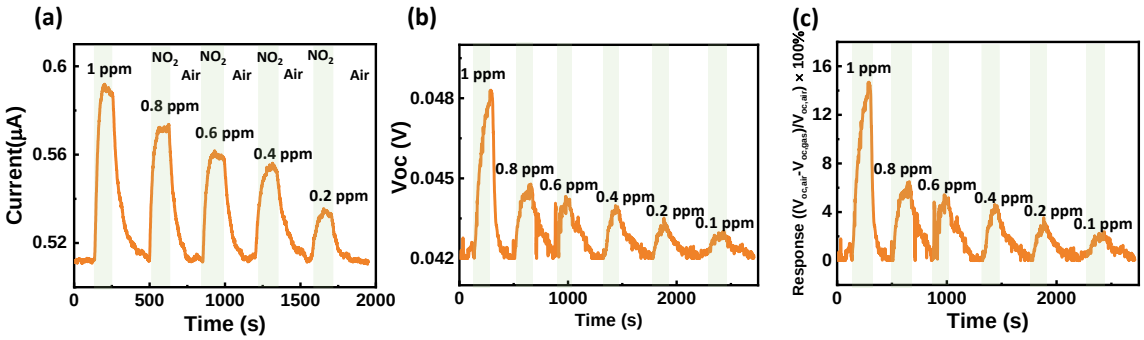

Figure S8. (a) Raw data from p-i-n InP NW photocurrent sensing measurement with concentration ranging from 0.2-1 ppm. (b, c) V_{OC} as output signal for the NO_2 sensing measurement and the corresponding calculated response with n-i-p sample.

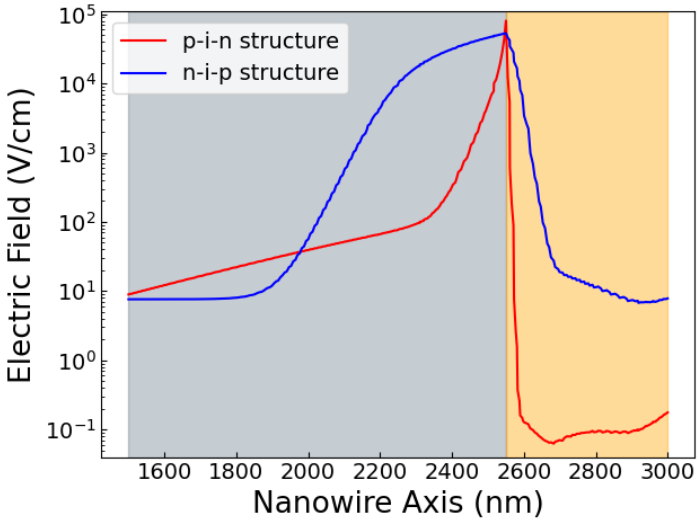

Figure S9. Electric field magnitude for p-i-n and n-i-p structures near the i-n/i-p junction. The thickness of top n/p segment is 450 nm. The grey shaded region indicates i-region and orange shaded region indicates the top segment.

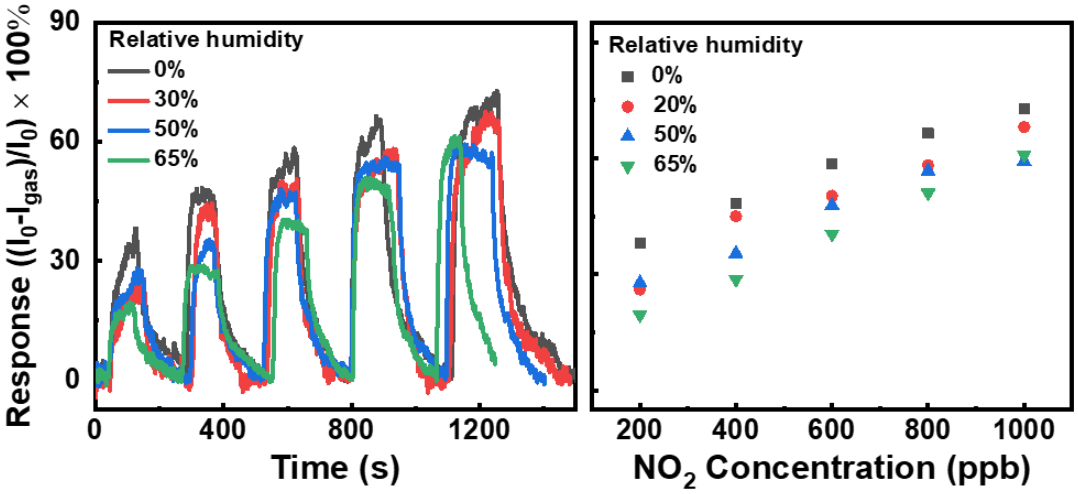

Figure S10. Time-dependent NO_2 sensing response from a p-i-n device under relative humidity (RH) 30%, 50%, 65% and the calculated response vs concentration result.

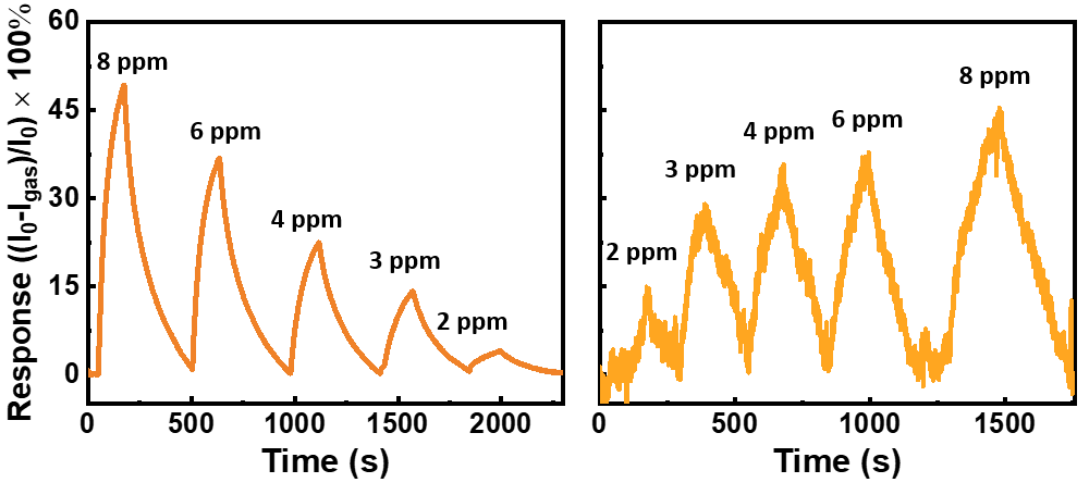

Figure S11. Concentration calibration measurement of the p-i-n NW sensor integrated on USB sensor interface. Left: measured with Linkam chamber lab gas sensing system; right: measured with JLMlogSP supplementary software together with USB interface. Due to the gas flow fluctuations and the intrinsic noise from the USB printed circuit, the on-filed measurement data exhibit much larger noise than the data measured by the lab gas sensing setup.

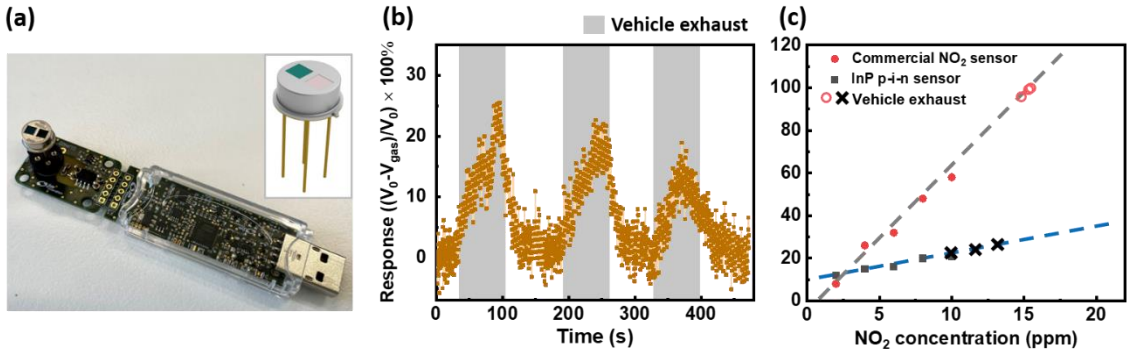

Figure 12. (a) The photos of commercial KEMET NO_2 (inset) integrated with the USB interface. (b) Sensing response was measured by connecting the commercial sensor with the USB interface; (c) The calibration between sensing response and NO_2 concentration for the commercial device was performed in the laboratory gas-sensing setup, shown in linear fitting; the on-field vehicle exhaust measurement (three times for each devices) is shown by circle and cross symbol indicating the range of NO_2 concentration calculated from the linear fitting.

Reference

[1] F. Wang, Q. Gao, K. Peng, Z. Li, Z. Li, Y. Guo, L. Fu, L. M. Smith, H. H. Tan and C. Jagadish, *Nano Lett.* **2015**, *15*, 3017-3023.

[2] Q. Gao, Z. Li, L. Li, K. Vora, Z. Li, A. Alabadla, F. Wang, Y. Guo, K. Peng, Y. C. Wenas, S. Mokkapati, F. Karouta, H. H. Tan, C. Jagadish and L. Fu, *Prog. Photovolt.: Res. Appl.* **2019**, *27*, 237-244.

[3] S. Y. Wei, Z. Li, A. John, B. I. Karawdeniya, Z. Y. Li, F. L. Zhang, K. Vora, H. H. Tan, C. Jagadish, K. Murugappan, A. Tricoli and L. Fu, *Adv. Funct. Mater.* **2022**, *32*, 2107596.

[4] J. Wallentin, M. T. Borgström, L. Samuelson, M. Ekawa and K. Kawaguchi, *Appl. Phys. Lett.* **2013**, *102*, 032105.

[5] V. Dagyte, E. Barrigon, W. Zhang, X. L. Zeng, M. Heurlin, G. Otnes, N. Anttu and M. T. Borgstrom, *Nanotechnology* **2017**, *28*, 505706.

[6] F. Wang, Q. Gao, K. Peng, Z. Li, Z. Y. Li, Y. N. Guo, L. Fu, L. M. Smith, H. H. Tan and C. Jagadish, *Nano Lett.* **2015**, *15*, 3017-3023.